Korean J. Chem. Eng., 32(10), 1970-1985 (2015)
DOI: 10.1007/s11814-015-0020-3

pISSN: 0256-1115
eISSN: 1975-7220

Magnetic field and throughflow effects on double-diffusive convection in internally heated anisotropic porous media

Akil Jassim Harfash*,† and Ahmed Kadhim Alshara**

*Department of Mathematics, College of Sciences, University of Basrah, Basrah, Iraq
**Petroleum Department, College of Engineering, University of Misan, Misan, Iraq
(*Received 29 December 2014 • accepted 23 January 2015*)

Abstract−A model for double-diffusive convection in an anisotropic porous layer with a constant throughflow is explored, with penetrative convection being simulated via an internal heat source and subjected to a vertical magnetic field and variable gravity effect. The validity of both the linear instability and global nonlinear stability thresholds are tested using three dimensional simulation. Our results show that the linear theory produce a good prediction on the onset of instability in the steady state throughflow. It is known that as R_c increases the onset of convection is more likely to be via oscillatory convection as opposed to steady convection, and the three dimensional simulation results show that as R_c increases, the actual threshold moving toward the nonlinear stability threshold and the behaviour of the perturbation of the solutions becomes more oscillated.

Keywords: Double-diffusive Convection, Throughflow, Internal Heat Source, Finite Differences, Anisotropic Porous Media

INTRODUCTION

Most available studies focus on the natural convection heat transfer through a porous medium saturated by an electrically nonconducting fluid, as in most practical situations. Recently, the equally important problem of hydromagnetic convective flow of a conducting fluid through a porous medium has been the centre of much investigation. Subjected to a magnetic field, the motion of an electrically conducting fluid induces an electric current whose fluid velocity is reduced, in general, by interaction between the electric current and the motion. The natural convection of electrically conducting fluids in porous media where a magnetic field exists has not, however, been the subject of much research, although there are potential applications. An example is the study of the interaction of the geomagnetic field with the fluid in geothermal regions, where the Earth's crust functions as a porous medium, is regarded by geophysicists as being of considerable importance. Also, with continuous casting, an example of metallurgical applications, electromagnetic stirring can improve the solidification structure to produce a fine-grained structure, with better final mechanical properties. Where dendritic solidification of alloys is concerned, dendrites in the mushy zone can be regarded as a porous medium. Some attention has been focussed on how a magnetic field affects the onset of instability in porous medium layers (cf. [1-3] and the references therein).

Double diffusive convection in porous media has been a focus for researchers, since it has applications in a number of areas, including geophysics, the enhanced recovery of petroleum reservoirs, the underground diffusion of chemical wastes, seabed hydrodynamics, and crystal growth. Nield and Bejan [4] have studied this to some depth, and there is a plentiful supply of other scientific literature dealing with the matter. In the porous layer, throughflow (the non-isothermal flow of fluids through porous media) occurs during the in-situ processing of energy resources such as coal, oil shale or geothermal energy and packed bed reactors. Research has recently been undertaken into the consequences of vertical throughflow on convective instability in a porous layer, cf. Nield [5], Shivakumara [6,7] and Shivakumara and Khalili [8].

Where practical issues are involved, control of double-diffusive convection in porous media is of significance, as in developing an effective method of waste material disposal and energy extraction. In this connection, various physical procedures can be employed, for example rotation and/or magnetic field or the use of non-uniform basic temperature gradients [9], which may occur owing to: transient heating or cooling at the boundaries, a uniform heat source in the porous layer, radiation heating and vertical throughflow. In a study by Rudraiah et al. [10], into the effect of the Coriolis force on double-diffusive convection in a sparsely packed porous medium it was found that the effect of the Taylor number at the marginal state was to increase the systems stability. However, in the case of overstability the bottom-heavy solute gradient and the Taylor number were shown to destabilise the system under certain conditions. The results in the case of rotation were similar to this in Shivakumaras [11], analysis of the corresponding double-diffusive magneto-convection problem.

The literature on the study of the effect of vertical throughflow on convective instability in a porous medium is much less widespread, although recent studies include Shivakumara and Suma [12], Shivakumara and Khalili [13], Shivakumara and Sureshkumar [14], Nield and Kuznetsov [15], Hill et al. [16] and Harfash and Hill [17].

However, the effects of vertical throughflow on double-diffusive convection in a porous medium are significant in applications

†To whom correspondence should be addressed.
E-mail: akilharfash@gmail.com

in engineering, geophysics and seabed hydrodynamics (for example, in hydrothermal vent systems). Although sufficient attention has not been given to the problem in research literature, its importance in the directional solidification of concentrated alloys, in which a porous layer with double diffusive origin, or a mushy zone, exists, is considerable.

The object of this paper is, therefore, to investigate the linear instability and nonlinear stability theories a of a porous layer with simultaneous temperature and solute concentration gradients for both strong and weak constant vertical flow and subjected to a vertical magnetic field. Assessing the onset and type of convection is crucial in understanding this system, which can be achieved by analysing both the linear instability and nonlinear stability thresholds of the governing model. Comparing these thresholds allows for the assessment of the suitability of linear theory to predict the physics of the onset of convection. In order to establish stability results we turn our attention to the highly adaptable energy method [18]. Nonlinear energy methods are particular useful as they delimit the parameter region of possible subcritical instability (the region between the linear instability and nonlinear stability thresholds). Hence, quantifying the discrepancy between these two thresholds makes it possible to provide an assessment of the suitability of linear theory to predict the de-stabilisation of the double diffusive convection in anisotropic porous media with throughflow, magnetic and variable gravity effects. Recent contributions on the study of convective instabilities in fluid and porous media include [19-31].

When the difference between the linear (which predicts instability) and nonlinear (which predicts stability) thresholds is very large, the validity of the linear instability threshold to capture the onset of the instability is unclear. Thus, we select regions of large subcritical instabiltiies and then develop a three dimensional simulation for the problem to test the validity of these thresholds. To achieve this we transform the problem into a vorticity-pseudostream function formulation and utilise second order finite difference schemes. Recently, in [32-36], the accuracy of the linear instability thresholds are tested using three-dimensional simulations. Our results show that the linear threshold accurately predicts on the onset of instability in the basic steady state. However, the required time to arrive at the steady state increases significantly as the Rayleigh number tends to the linear threshold.

In the next section, we present the governing equations of motion and derive the associated perturbation equations. In Section 3, we introduce the linear and nonlinear analysis of our system. In Section 4, we introduce the numerical technique to solve the eigenvalue systems. In Section 5, the numerical results for the linear theory and a direct comparison with those of the global nonlinear theories are presented. In Section 6, we transform our system to the vorticity-pseudostream function formulation and introduce the numerical solution of the problem in three dimensions. The three dimensions results of our numerical Model are then compiled and discussed in the final section of the paper.

MATHEMATICAL FORMULATION AND GOVERNING EQUATIONS

Let us consider a layer Ω of a water saturated porous medium

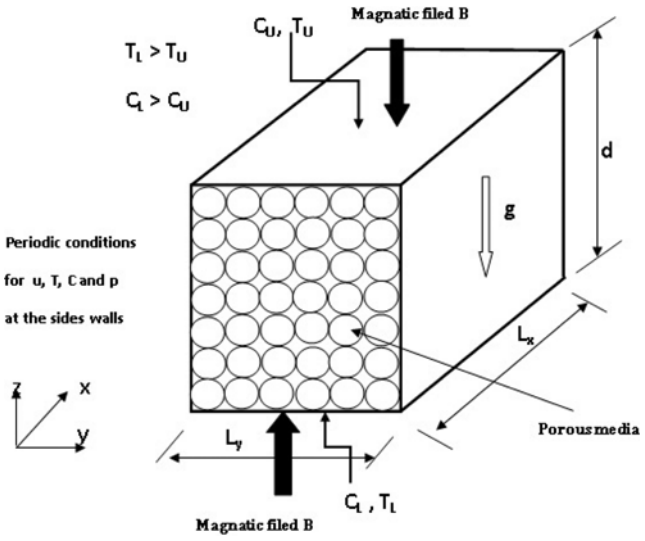

Fig. 1. A schematic of the physical domain.

bounded by two horizontal planes as shown in Fig. 1. Let d>0, $\Omega = \mathbb{R}^2 = (0, d)$ and Oxyz be a Cartesian frame of reference with unit vectors i, j, k. Denoting **v**, T and C to be the velocity, temperature and concentration of the dissolved species. The porous medium in the box with porosity ε. The fluid is subjected to the buoyancy forces resulting from temperature difference ($T_L - T_U$) and the diffusion of mass due to the concentration difference ($C_L - C_U$) between the upper and lower planes where $T_L > T_U$ and $C_L > C_U$, behind that the electromagnetic force resulting from convection of fluid in an uniform magnetic field. The diffusion in the box is unsteady and three-dimensional, subject to a uniform magnetic field B. We assume that the variables (u, T, C and p) are periodic in the x and y directions with periodically cells. Also, assuming that the Oberbeck-Boussinesq approximation is valid (cf. [4] and [18] and references therein), the flow in the porous medium is governed by Darcy's law

$$\frac{\mu}{K(z)} v_i = -P_{,i} - k_i g(z)\rho(T, C) + \mathbf{J} \times \mathbf{B}, \tag{1}$$

$$v_{i,i} = 0, \tag{2}$$

$$\frac{1}{\mathcal{M}} T_{,t} + v_i T_{,i} = \kappa_t \nabla^2 T + Q, \tag{3}$$

$$\varepsilon C_{,t} + v_i C_{,i} = \kappa_c \nabla^2 C, \tag{4}$$

where (2) is the incompressibility condition and (3) and (4) are the equations of energy and solute balance, respectively. The derivation of Eqs. (1)-(4) may be found in [4].

We have denoted P, μ, ε, g, **J**, **B** and κ_c to be the pressure, viscosity, porosity, gravitational acceleration, current, magnetic induction field and salt diffusivity, respectively. The density ρ is of the form

$$\rho(T, C) = \rho_0(1 - \alpha_t(T - T_0) + \alpha_c(C - C_0))$$

where ρ_0, T_0 and C_0 are a reference density, temperature and concentration, respectively, and α_t and α_c are the coefficients for thermal and solutal expansion, respectively.

The permeability of the porous medium is taken to be of the form

$$K(z)=K_0 s(z),$$

where K_0 is a reference permeability and $s(z)=1+\lambda_1 z/d$, with constant $\lambda_1>-1$ to ensure $s(z)>0$. The effective thermal conductivity of the saturated porous medium κ_t is defined by the ratio between the thermal diffusivity of the porous medium and the heat capacity per unit volume of the fluid:

$$\kappa_t=\frac{(1-\varepsilon)\kappa_s+\varepsilon\kappa_f}{(\rho_0 c_p)_f}$$

where κ_s and κ_f are the thermal diffusivities of the solid and fluid components of the porous medium, respectively and c_p is the specific heat of the fluid at constant pressure. The coefficient $\mathcal{M}$ is the ratio of heat capacities defined by

$$\mathcal{M}=\frac{(\rho_0 c_p)_f}{(\rho_0 c)_m}. \tag{5}$$

In (5) c is the specific heat of the solid, and

$$(\rho_0 c)_m=(1-\varepsilon)(\rho_0 c)_s+\varepsilon(\rho_0 c_p)_f,$$

denotes the overall heat capacity per unit volume of the porous medium. The subscripts f, s and m referring to the fluid, solid and porous components of the medium, respectively.

The Q (>0) term in (3) is a (constant) internal heat source, with its inclusion allowing the model to describe penetrative convection in the porous layer.

Convectional hydrodynamic stability theory is mainly concerned with the determination of critical values of Rayleigh number, demarcating a region of stability from that of instability. To make the convective overturning instability problem tractable we employ the quasi-static MHD approximation of Galdi and Straughan [37]. This assumes that the electric field, **E**, may be derived from a potential $\mathbf{E}=-\nabla\chi$. The magnetic field **H** and the electric field satisfy Maxwell's equations, cf. Roberts [38], Fabrizio and Morro [39], so that

$$curl\ \mathbf{H}=\mathbf{J},\quad curl\ \mathbf{E}=-\frac{\partial \mathbf{B}}{\partial t}.$$

Here $\mathbf{B}=\mu\mathbf{H}$ and then Galdi and Straughan [37] show that if the vertical component in the perturbed motion is zero in the limit magnetic Prandtl number $P_m=\nu/\eta\to 0$, where η is the resistivity, then $\mathbf{J}\times\mathbf{B}$ in Eq. (1) may be replaced by

$$\mathbf{J}\times\mathbf{B}=\sigma_1(\mathbf{v}\times\mathbf{B}_0)\times\mathbf{B}_0, \tag{6}$$

where σ_1 is the electrical conductivity and $\mathbf{B}_0=(0, 0, B_0)$ is a magnetic field with only the vertical component. We now employ (6) in (1).

The temperature and concentration boundary conditions for the problem are $T=T_U$ and $C=C_U$ at z=d and $T=T_L$ and $C=C_L$ at z=0, where $T_L>T_U$ and $C_L>C_U$, so that the system is being heated and salted from below.

Let us now consider the basic steady state solution of (1)-(4), with a throughflow in the z direction of the form

$$\bar{\mathbf{v}}=(0, 0, V),$$

where V is constant. Utilising the boundary conditions, Eqs. (3) and (4) yield the temperature and concentration steady states

$$\overline{T}(z)=\frac{Qz}{V}+T_L+\frac{V(T_L-T_U)+Qd}{V(e^{Vd/\kappa_t}-1)}(1-e^{Vz/\kappa_t}),$$

$$\overline{C}(z)=C_L+\frac{C_L-C_U}{1-e^{Vd/\kappa_c}}(e^{Vz/\kappa_c}-1).$$

To investigate the stability of these solutions, we introduce perturbations (u_i, p, θ, ϕ) by

$$v_i=u_i+\bar{v}_i,\quad P=p+\overline{P},\quad T=\theta+\overline{T},\quad C=\phi+\overline{C}.$$

The perturbation equations are nondimensionalized according to the scales (stars denote dimensionless quantities)

$$p=\frac{\mu\kappa_t}{K_0}p^*,\quad \theta=\theta^*\sqrt{\frac{dQ\mu}{\rho_0\alpha_t K_0}},\quad x_i=dx_i^*,\quad \phi=\phi^*\sqrt{\frac{\mu\kappa_t(C_L-C_U)}{\rho_0\alpha_c K_0 d}},$$

$$u_i=\frac{\kappa_t}{d}u_i^*,\quad t=\frac{d^2}{\kappa_t\mathcal{M}}t^*,\quad \hat{\varepsilon}=\mathcal{M}\varepsilon,\quad Le=\frac{\kappa_t}{\kappa_c},\quad T_f=\frac{Vd}{\kappa_t},$$

$$R_t^2=\frac{\rho_0\alpha_t K_0 d^3 Q}{\mu\kappa_t^2},\quad R_c^2=\frac{\rho_0\alpha_c K_0 d(C_L-C_U)}{\mu\kappa_t},$$

$$\varepsilon=\frac{(T_L-T_U)\kappa_t}{Qd^2},\quad M=B_0\sqrt{\frac{\sigma_1\kappa}{\mu}},$$

where R_t^2 and R_c^2 are the thermal and solute Rayleigh numbers, respectively, and T_f is the non-dimensional form of the throughflow. The dimensionless perturbation equations are (after omitting all stars)

$$\frac{1}{f(z)}u_i=-p_{,i}+R_t g(z)\theta k_i-R_c g(z)\phi k_i+M^2[(u\times k)\times k]_i, \tag{7}$$

$$u_{i,i}=0, \tag{8}$$

$$\theta_{,t}+u_i\theta_{,i}+T_f\theta_{,3}=R_t f_1(z)w+\nabla^2\theta, \tag{9}$$

$$\hat{\varepsilon}\phi_{,t}+u_i\phi_{,i}+T_f\phi_{,3}=R_c f_2(z)w+\frac{1}{Le}\nabla^2\phi, \tag{10}$$

with $w=u_3$ and $f(z)=1+\lambda z$ (with $\lambda>-1$ to ensure $f(z)>0$),

$$f_1(z)=\frac{T_f}{e^{T_f}-1}\left(\varepsilon+\frac{1}{T_f}\right)e^{T_f z}-\frac{1}{T_f},$$

$$f_2(z)=\frac{LeT_f e^{LeT_f z}}{e^{LeT_f}-1}.$$

It is important to note that $\varepsilon>0$ and $\varepsilon<0$ correspond to heating from below and above, respectively. These equations hold in the region $\{z\in 2\ (0, 1)\}\times\{(x, y)\in\mathbb{R}^2\}$ and the boundary conditions to be satisfied are:

$$\mathbf{u}=0,\ \theta=0,\ \phi=0,\ \text{at } z=0, 1, \tag{11}$$

where u_i, p, θ and ϕ are assumed periodic in the x and y directions.

LINEAR AND NONLINEAR STABILITY THEORIES

To obtain the threshold for linear instability where we know convection occurs we neglect the nonlinear terms in Eqs. (7)-(10). Then, due to linearity we may seek solutions like $u_i(\mathbf{x}, t)=u_i(\mathbf{x})e^{\sigma t}$, $\theta(\mathbf{x},$

$t)=\theta(\mathbf{x})e^{\sigma t}$, $\phi(\mathbf{x}, t)=\phi(\mathbf{x})e^{\sigma t}$ and $\mathcal{P}(\mathbf{x}, t)=\mathcal{P}(\mathbf{x})e^{\sigma t}$, where σ is a complex constant. This leads to the system

$$\frac{1}{f(z)}u_i=-\pi_{,i}+R_t g(z)\theta k_i-R_c g(z)\phi k_i+M^2[(\mathbf{u}\times\mathbf{k})\times\mathbf{k}]_i, \tag{12}$$

$$\sigma\theta=\Delta\theta+R_t f_2(z)w. \tag{13}$$

$$\hat{\varepsilon}\sigma\phi=\Delta\phi+R_c f_2(z)w. \tag{14}$$

To proceed further we then take *curlcurl* of (12), and retain the third component of the resulting equation, namely

$$0=-\frac{1}{f(z)}\Delta w+\frac{f'(z)}{f^2(z)}w_{,z}+R_t g(z)\Delta^*\theta-R_c g(z)\Delta^*\phi-M^2D^2w, \tag{15}$$

where $\Delta^*=\partial^2/\partial x^2+\partial^2/\partial y^2$ and $D=d/dz$.

Next, due to the periodicity of the solution in the (x, y) variables we may write w and ϕ as

$w=W(z)h(x, y)$, $\theta=\Theta(z)h(x, y)$ and $\phi=\Phi(z)h(x, y)$,

where h is a plane-tiling planform so that

$$\Delta^*h=-a^2h, \tag{16}$$

where a is the wavenumber. Such planforms are discussed in detail in [?], p.43-52 and [18], p.51. Eqs. (13)-(15) reduce to

$$f(z)(D^2-a^2)W-f'(z)DW+a^2R_t f^2(z)g(z)\Theta - a^2R_c f^2(z)g(z)\phi+M^2f^2(z)D^2W=0, \tag{17}$$

$$(D^2-a^2)\Theta-T_f D\Theta+R_t f_1(z)W=\sigma\Theta, \tag{18}$$

$$\frac{1}{Le}(D^2-a^2)\phi-T_f D\phi+R_c f_2(z)W=\hat{\varepsilon}\sigma\phi, \tag{19}$$

System (17)-(19) represents an eigenvalue problem for the eigenvalues σ.

When adopting a linear analysis approach, the perturbation to the steady state is assumed to be small, and so nonlinear terms in the governing set of partial differential equations are discarded. It has been proved that linear analysis often provides little information on the behavior of the nonlinear system [18], so in such cases only instability can be deduced from the linear thresholds, as any potential growth in the nonlinear terms is not considered.

To develop a nonlinear stability analysis, let V be a period cell for the disturbance solution in Eqs. (7)-(10). Let $\|\cdot\|$ and $(\cdot, \cdot)$ be the norm and inner product on the Hilbert space $L^2(V)$. We multiply Eq. (7) by u_i and integrate over V. After some integrations by parts, use of the boundary conditions (11), and employing Eq. (8) we derive the identity

$$0=-\left(\mathbf{u}, \frac{1}{f}\mathbf{u}\right)+R(w, g\theta)-R_c(w, g\phi)-M^2(|\mathbf{u}|^2-|w|^2). \tag{20}$$

Next, multiply Eqs. (9) and (10) by θ and ϕ, then integrate over V, to see that after further integrations by parts and use of (8) and (11), we obtain

$$\frac{1}{2}\frac{d}{dt}|\theta|^2=R(f_1w, \theta)-|\nabla\theta|^2. \tag{21}$$

$$\frac{\hat{\varepsilon}}{2}\frac{d}{dt}|\phi|^2=R_c(f_2w, \phi)-|\nabla\phi|^2. \tag{22}$$

The idea is to now add (20)+λ_1 (21)+λ_2 (22) for positive parameters λ_1 and λ_2 which we later select optimally. This leads to the energy equation

$$\frac{dE}{dt}=\mathcal{I}-\mathcal{D}, \tag{23}$$

where E, $\mathcal{I}$ and $\mathcal{D}$ are defined by

$$\begin{aligned} E(t)&=\frac{\lambda_1}{2}|\theta|^2+\hat{\varepsilon}\frac{\lambda_2}{2}|\phi|^2,\\ \mathcal{I}&=R_t(w, \theta[g+\lambda_1f_1])-R_c(w, \phi[g-\lambda_2f_2]),\\ \mathcal{D}&=\left(\mathbf{u}, \frac{1}{f}\mathbf{u}\right)+\lambda_1|\nabla\theta|^2+\lambda_2|\nabla\phi|^2+M^2(|\mathbf{u}|^2+|v|^2), \end{aligned} \tag{24}$$

where $\mathbf{u}$ is explicitly written as $\mathbf{u}=(u, v, w)$. Define now

$$\frac{1}{R_E}=\max_{\mathcal{H}}\frac{\mathcal{I}}{\mathcal{D}}, \tag{25}$$

where $\mathcal{H}$ is the space of admissible solutions and then from (23) we find

$$\frac{dE}{dt}\le-\mathcal{D}\left(1-\frac{1}{R_E}\right), \tag{26}$$

If $R_E>1$ then with χ_1 being the constant in poincare's inequality, it follows that $\mathcal{D}>cE$ where $c=\min\{2(\chi_1+\xi^2)p_s^{-1}, 2\chi_1p_r^{-1}\}$. Hence it follows that

$$\frac{dE}{dt}\le-cE\left(\frac{R_E-1}{R_E}\right).$$

Thus, letting $\varrho=c(R_E-1)/R_E$ we have $E(t)\le E(0)e^{-\varrho t}$ which tends to 0 as $t\to\infty$, so we have shown the decay of ϕ, θ and $\mathbf{u}$.

The Euler-Lagrange equations which arise from (25) are:

$$\frac{-2}{f}u_i+R_tk_i(g+\lambda_1f_1)\theta-R_ck_i(g-\lambda_2f_2)\phi-2M^2(u_i-k_iw)=\zeta_{,i}, \tag{27}$$

$$2\lambda_1\Delta\theta+R_t(g+\lambda_1f_1)w=0, \tag{28}$$

$$2\lambda_2\Delta\phi-R_c(g-\lambda_2f_2)w=0, \tag{29}$$

where ζ is a lagrange multiplier. To solve the energy eigenvalue problem (27)-(29) we remove the ζ term by taking *curlcurl* of (27) to arrive at the system

$$\frac{-2}{f}\Delta w+\frac{2f'}{f^2}w_{,z}-2M^2w_{,zz}+R_t(g+\lambda_1f_1)\Delta^*\theta - R_c(g-\lambda_2f_2)\Delta^*\phi=0, \tag{30}$$

$$2\lambda_1\Delta\theta-R_t(g+\lambda_1f_1)w=0. \tag{31}$$

$$2\lambda_2\Delta\phi-R_c(g-\lambda_2f_2)w=0. \tag{32}$$

Again, the representations $w=W(z)h(x, y)$, $\theta=\Theta h(x, y)$ and $\phi=\Phi(z)h(x, y)$ are introduced and we solve (30)-(32) as

$$2f(D^2-a^2)W-2DfDW+2M^2f^2D^2W-a^2R_tf^2(g-\lambda_2f_2)\Phi =-a^2R_tf^2(g+\lambda_1f_1)\Theta, \tag{33}$$

$$2\lambda_1(D^2-a^2)\Theta=-R_t(g+\lambda_1f_1)W, \tag{34}$$

$$2\lambda_2(D^2-a^2)\Phi-R_c(g-\lambda_2f_2)W=0, \tag{35}$$

together with boundary conditions (19). Numerical results are presented in the next section.

NUMERICAL TECHNIQUE

In this section, we use the Chebyshev collocation method to solve the eigenvalue systems (17)-(18) and (33)-(35). Firstly, the systems is transformed onto the Chebyshev domain (−1, 1) and the solutions W, θ and ϕ treated as independent variables and expanded in a series of Chebyshev polynomials

$$W=\sum_{n=0}^{N} w_n T_n(z),\quad \Theta=\sum_{n=0}^{N} \Theta_n T_n(z),\quad \Phi=\sum_{n=0}^{N} \Phi_n T_n(z), \tag{36}$$

then, we insert (36) into the Eqs. (17)-(18), and then substitute the Gauss-Labatto points which are defined by

$$y_i=\cos\left(\frac{\pi i}{N-3}\right),\quad i=0,\ \ldots,\ N-2. \tag{37}$$

Thus, we obtain 3N−3 algebraic equations for 3N+3 unknowns $W_0, \ldots, W_N, \Theta_0, \ldots, \Theta_N, \Phi_0, \ldots, \Phi_N$. Now, we can add six rows using the boundary conditions (19) as follows

$$BC_1:\sum_{n=0}^{N} W_n=0,\quad BC_2:\sum_{n=0}^{N}(-1)^n W_n=0,\quad BC_3:\sum_{n=0}^{N}\Theta_n=0,$$
$$BC_4:\sum_{n=0}^{N}(-1)^n\Theta_n=0,\quad BC_5:\sum_{n=0}^{N}\Phi_n=0,\quad BC_6:\sum_{n=0}^{N}(-1)^n\Phi_n=0.$$

The inner product of each equation is taken with some T_k and the orthogonality of the Chebyshev polynomials exploited to obtain the following generalised eigenvalue problem.

$$\begin{pmatrix} \Omega_1 & a^2R_t\Sigma & -a^2R_c\Sigma \\ BC_1 & 0\ldots0 & 0\ldots0 \\ BC_2 & 0\ldots0 & 0\ldots0 \\ R_t\gamma_1 & \Omega_2 & O \\ 0\ldots0 & BC_3 & 0\ldots0 \\ 0\ldots0 & BC_4 & 0\ldots0 \\ R_c\gamma_2 & O & \Omega_2 \\ 0\ldots0 & 0\ldots0 & BC_5 \\ 0\ldots0 & 0\ldots0 & BC_6 \end{pmatrix} X=\sigma \begin{pmatrix} O & O & O \\ 0\ldots0 & 0\ldots0 & 0\ldots0 \\ 0\ldots0 & 0\ldots0 & 0\ldots0 \\ O & I & O \\ 0\ldots0 & 0\ldots0 & 0\ldots0 \\ 0\ldots0 & 0\ldots0 & 0\ldots0 \\ O & O & \hat{\varepsilon}I \\ 0\ldots0 & 0\ldots0 & 0\ldots0 \\ 0\ldots0 & 0\ldots0 & 0\ldots0 \end{pmatrix} X, \tag{38}$$

where $X=(W_0, \ldots, W_N, \Theta_0, \ldots, \Theta_N, \Phi_0, \ldots, \Phi_N)$, O is the zeros matrix, $I(n_1, n_2)=T_{n_2}(z_{n_1})$, $D(n_1, n_2)=T'_{n_2}(z_{n_1})$, $D^2(n_1, n_2)=T''_{n_2}(z_{n_1})$, $\gamma_1(n_1, n_2)=f_1(z_{n_1})I(n_1, n_2)$, $\gamma_2(n_1, n_2)=f_2(z_{n_1})I(n_1, n_2)$, $\Sigma(n_1, n_2)=f_2(z_{n_1})g(z_{n_1})I(n_1, n_2)$, $\Omega_1=f(z_{n_1})(4D^2(n_1, n_2)-a^2I(n_1, n_2))-2f'(z_{n_1})D+M^2f^2(z_{n_1})D^2(n_1, n_2)$, $\Omega_2=4D^2(n_1, n^2)-a^2I(n_1, n_2)-2T_fD(n_1, n_2)$, $n_1=0, \ldots, N-2$, $n_2=0, \ldots, N$. We computed the differentiation matrices, which are corresponded to the trail functions (36) analytically using Matlab routines.

We have solved system (38) for eigenvalues σ_j by using the QZ algorithm from Matlab routines. Once the eigenvalues σ_j are found we use the secant method to locate where σ_j^R, $\sigma_j=\sigma_j^R+\sigma_j^I$ being the real and imaginary parts of eigenvalue σ_j. The value of R which makes $\sigma_1^R=0$, σ_1^R being the largest eigenvalue, is the critical value of R for a^2 fixed. We then use golden section search to minimize over a^2 and find the critical value of R^2 for linear instability. Numerical results are reported in the next section. In our use of the Chebyshev collocation method, we used polynomial of degree between 20 and 30. Usually 25 was found to be sufficient but convergence was checked by varying the degree by examining the convergence of the associated eigenvector (which yields the approximate associated eigenfunction).

Returning to the nonlinear eigenvalue system (33)-(35), the the Chebyshev collocation method yields

$$\begin{pmatrix} \Omega_1 & O & -0.5a^2R_c\Lambda_{22} \\ BC_1 & 0\ldots0 & 0\ldots0 \\ BC_2 & 0\ldots0 & 0\ldots0 \\ O & 2\lambda_1\Omega_2 & O \\ 0\ldots0 & BC_3 & 0\ldots0 \\ 0\ldots0 & BC_4 & 0\ldots0 \\ -R_c\Lambda_{21} & O & 2\lambda_2\Omega_2 \\ 0\ldots0 & 0\ldots0 & BC_5 \\ 0\ldots0 & 0\ldots0 & BC_6 \end{pmatrix} X=R_t \begin{pmatrix} O & -0.5a^2\Lambda_{12} & O \\ 0\ldots0 & 0\ldots0 & 0\ldots0 \\ 0\ldots0 & 0\ldots0 & 0\ldots0 \\ -\Lambda_{11} & O & O \\ 0\ldots0 & 0\ldots0 & 0\ldots0 \\ 0\ldots0 & 0\ldots0 & 0\ldots0 \\ O & O & O \\ 0\ldots0 & 0\ldots0 & 0\ldots0 \\ 0\ldots0 & 0\ldots0 & 0\ldots0 \end{pmatrix} X. \tag{39}$$

where

$$\Lambda_{11}(n_1, n_2)=(\lambda_1 f_1(z_{n_1})+g(z_{n_1}))I(n_1, n_2),$$
$$\Lambda_{12}(n_1, n_2)=f^2(z_{n_1})(\lambda_1 f_1(z_{n_1})+g(z_{n_1}))I(n_1, n_2),$$
$$\Lambda_{21}(n_1, n_2)=(-\lambda_2 f_2(z_{n_1})+g(z_{n_1}))I(n_1, n_2)$$

and

$$\Lambda_{22}(n_1, n_2)=f^2(z_{n_1})(-\lambda_2 f_2(z_{n_1})+g(z_{n_1}))I(n_1, n_2)$$

Then, we can determine the critical Rayleigh Ra_E for fixed a^2, λ_1 and λ_2. Next, we employ golden section search to minimize in a^2 and then maximize in λ_1 and λ_2 to determine Ra_E for nonlinear energy stability,

$$Ra_E=\max_{\lambda_1,\,\lambda_2}\ \min_{a^2} R^2(a^2, \lambda_1, \lambda_2), \tag{40}$$

where for all $R^2<Ra_E$ we have stability. In fact, the optimization problem (40) turns out to be very tricky. Numerically it was found that there are local maxima and one has to be very careful when searching to locate a maximum which is useful. Numerical results are reported in the next section and compared to those of linear instability theory.

STABILITY ANALYSIS RESULTS

The numerical results are presented for the gravity field $g(z)=1-\varepsilon_1 z$, while the numerical routine is applicable to a wide variety

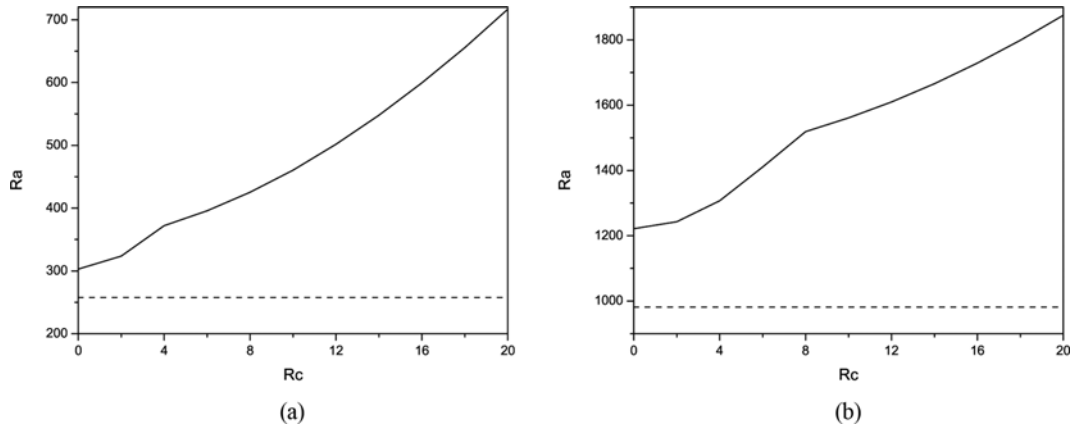

Fig. 2. Visual representation of stationary linear instability (solid line) and nonlinear stability (dashed line) thresholds, with critical Rayleigh number plotted against R_c, where T_f=1, ε=0.1 and (a) λ=0, M^2=0, ε_1=0, (b) λ=0.5, M^2=5, ε_1=0.5.

of other fields. To investigate the possibility of a very widely varying gravity field (one which even changes sign) we choose ε_1 to vary from 0 to 1.8. The results in this paper are given for $\hat{\varepsilon}$=5 and Le=1.

The thresholds of both the numerical linear instability and nonlinear stability results are presented in Fig. 2. More comparable linear and nonlinear thresholds are apparent as the onset of convection predicted by the linear theory becomes fully stationary. However, their agreement does deteriorate as the solute Rayleigh number becomes large, indicating that the linear theory may fail to suitably emulate the physics of the onset of convection. The behaviour of the linear instability curves is in good agreement with that seen in [40]. The kink in the curves represents the point at which convection switches from steady convection (σ=0) to oscillatory (σ_r=0, $\sigma_i \neq 0$). Note that as R_c increases the onset of convection is more likely to be via oscillatory convection as opposed to steady convection. We observe from Fig. 2 that for R_c=0 there is very good agreement between the nonlinear stability and linear instability bounds. We also note that as R_c is small the linear and nonlinear results become closer and remark that since the critical Rayleigh numbers are so close (for R_c sufficiently small) we expect the linear analysis to have captured the essential physics of the onset of convection. However as R_c increases the agreement between the two thresholds is not so good and we highlight this area as a region of possible subcritical instabilities.

Fig. 3 gives a visual representation of the linear instability and nonlinear stability thresholds, with critical thermal Rayleigh number Ra plotted against the magnetic field. The remaining parameters are held fixed at T_f=1, ε=0.1, λ=0.5, ε_1=0.5, R_c=6. This figure shows the effect of increasing M^2 on the critical Rayleigh number. It is clear from this figure that an increase in M^2 causes the system the become more stable, which we would physically expect. For M^2>4, the stationary convection become dominator in the linear instability thresholds. When $M^2 \leq 4$, the oscillatory modes become present in the linear instability thresholds. Fig. 3 demonstrates that Ra increases with increasing M^2 which shows the stabilizing effect of M^2. It is very noteworthy that the nonlinear stability curves are

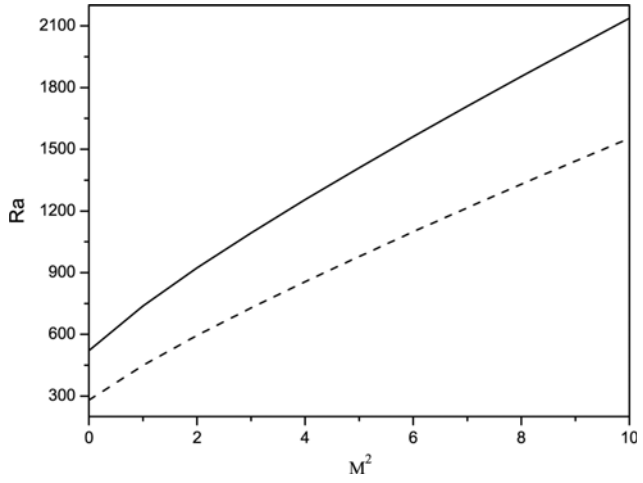

Fig. 3. Visual representation of stationary linear instability (solid line), oscillatory linear instability (dashed line) and nonlinear stability (dotted line) thresholds, with critical Rayleigh number plotted against M^2, where T_f=1, ε=0.1, λ=0.5, ε_1=0.5, R_c=6.

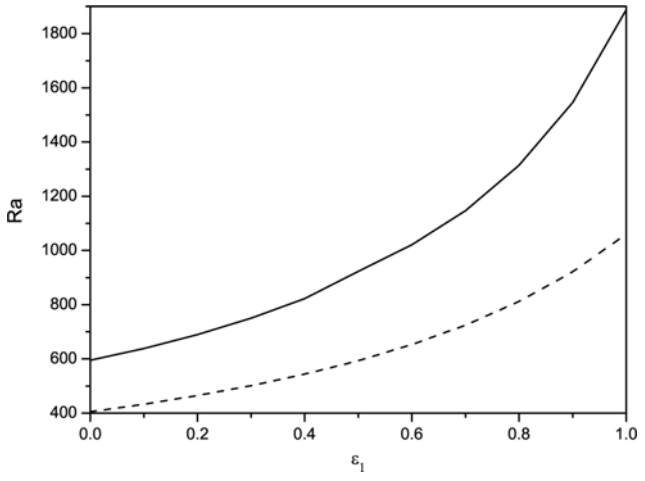

Fig. 4. Visual representation of stationary linear instability (solid line), oscillatory linear instability (dashed line) and nonlinear stability (dotted line) thresholds, with critical Rayleigh number plotted against ε_1, where T_f=1, ε=0.1, λ=0.5, M^2=2, R_c=6.

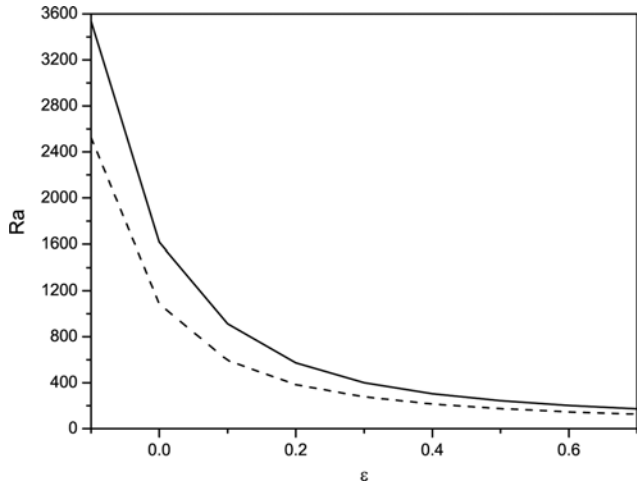

Fig. 5. Visual representation of stationary linear instability (solid line), oscillatory linear instability (dashed line) and nonlinear stability (dotted line) thresholds, with critical Rayleigh number plotted against ε, where T_f=1, λ=0.5, M^2=2, ε_1=0.5, R_c=6.

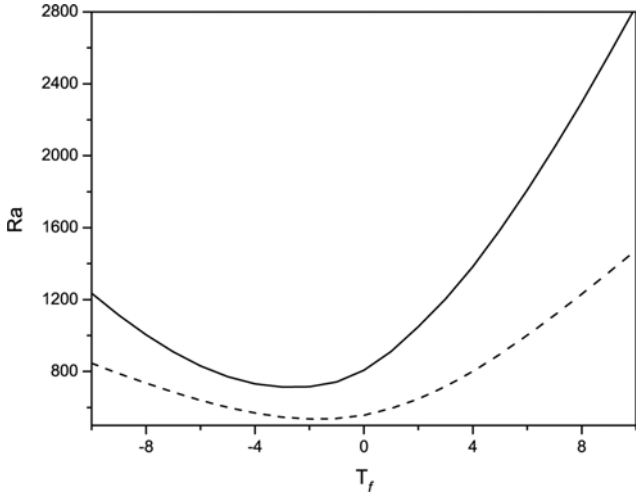

Fig. 7. Visual representation of stationary linear instability (solid line), oscillatory linear instability (dashed line) and nonlinear stability (dotted line) thresholds, with critical Rayleigh number plotted against T_f, where ε=0.1, λ=0.5, M^2=2, ε_1=0.5, R_c=6.

close to those of linear theory. This shows that possible sub-critical instabilities may arise in a small range of Rayleigh numbers, and it also demonstrates that linear instability theory does correctly capturing the physics of the onset of convection. It is worth pointing out that such stabilizing effect of the magnetic field has been observed in [1-3].

Fig. 4 gives a visual representation of the linear instability and nonlinear stability boundaries, with critical thermal Rayleigh number Ra plotted against ε_1. The remaining parameters are held fixed at T_f=1, ε=0.1, λ=0.5, M^2=2, R_c=6. It is clear from this figure that Ra increases with increasing ε_1 which refers to the stabilizing effect of ε_1. It is clearly demonstrated in these figures that for small values of ε the linear and non-linear thresholds have substantial correlation, demonstrating the suitability of linear theory to predict the physics of the onset of convection. As ε increased the thresholds have less correlation.

Fig. 5 shows how increasing ε, corresponds, to destabilization. It is clear from Fig. 5 that an increase in ε causes the system the become more unstable, which we would physically expect. Again, it is very noticeable that the nonlinear energy stability curves are close to those of linear instability. This is reinforcing the fact that the linear curves are true representation that the physics of the onset of convection is being correctly reflected. The gap between the curves represents the small band where sub-critical bifurcation may possibly occur. For ε<0, the stationary convection become dominator in the linear instability thresholds. However, for ε≥0, the oscillatory convection appears in the linear instability.

A visual representation of the influence of λ on the critical Rayleigh numbers of linear instability and global nonlinear stability is given in 6. From 6 we observe that changes in the value of λ does have a significant impact on the shape of the neutral curves. As one would physically expect, λ<0 is more stable than λ>0 as the permeability is decreasing (as opposed to increasing) from the bottom to the top layer, inhibiting the flow. For T_f=1, it is interesting to note that

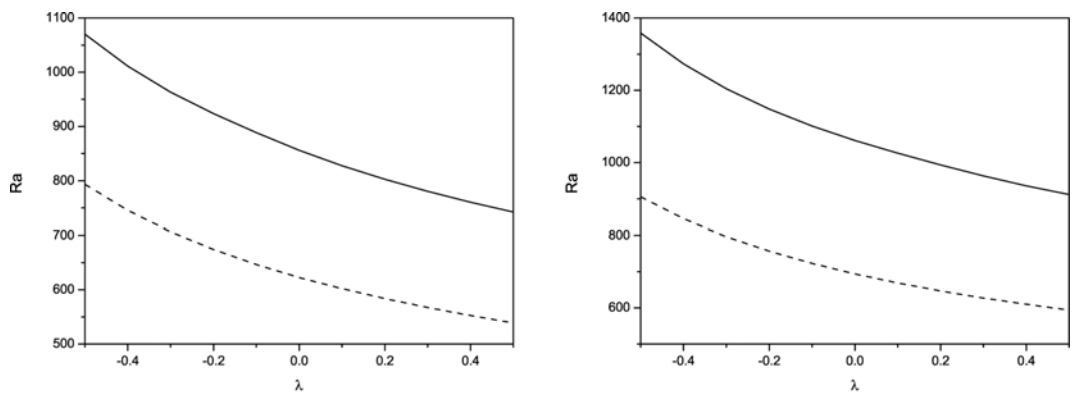

(a) $T_f = -1$ (b) $T_f = 1$

Fig. 6. Visual representation of stationary linear instability (solid line), oscillatory linear instability (dashed line) and nonlinear stability (dotted line) thresholds, with critical Rayleigh number plotted against λ, where ε=0.1, M^2=2, ε_1=0.5, R_c=6.

the oscillatory and stationary modes become present in the linear instability thresholds, for $\lambda \geq 0.1$ and $\lambda < 0.1$, respectively. Also, For $T_f = -1$, the oscillatory convection appears in the linear instability when $\lambda \geq 0$ while the stationary convection in linear instability become dominator for $\lambda < 0$.

A visual representation of the linear instability and global nonlinear stability thresholds is given in 7. To assist in the interpretation of the results, we recall that ascending and descending throughflow are represented by the positivity and negativity of the value of T_f, respectively. Fig. 7 clearly demonstrate that the linear and nonlinear thresholds have excellent agreement for $0 \leq T_f \leq 4$. When Q is negative the thresholds demonstrate less substantial agreement. This pattern of results is similar to the behaviour of throughflow in a fluid layer (cf. [41]). For $-2 \leq T_f \leq 3$, the oscillatory convection become dominator in the linear instability thresholds, and otherwise, the stationary convection appears in the linear instability. A similar structure is observed in the case where the density is quadratic in temperature [16].

VORTICITY-PSEUDOSTREAM FUNCTION FORMULATION

In Sections 6 and 4 we now develop a three-dimensional approach to solve the time dependent governing Eqs. (1)-(4) in order to assess the accuracy of the linear instability and nonlinear stability thresholds. A schematic diagram of the three-dimensional space (based on Fig. 1) under consideration is given in Section 7.

In this paper, we present an efficient, stable, and accurate finite difference schemes in the vorticity-vector potential formulation for computing the convective motion of an incompressible fluid in a porous material. The emphasis is on three dimensions and nonstaggered grids. We introduce a second-order accurate method based on the vorticity-vector potential formulation on the nonstaggered grid whose performance on uniform grids is comparable with the finite scheme. We will pay special attention to how accurately the divergence-free conditions for vorticity, velocity, and vector potential are satisfied. We will derive the three-dimensional analog of the local vorticity boundary conditions.

By using the curl operator to Eq. (7), one gets the following dimensionless form of the vorticity transport equation:

$$\frac{1}{f(z)}\vec{\omega} - \frac{f'(z)}{f^2(z)}(-v,\, u,\, 0) = R\nabla\times\theta\mathbf{k} - R_c\nabla\times\phi\mathbf{k} + M^2\nabla\times w\mathbf{k}. \tag{41}$$

where the vorticity vector $\vec{\omega}=(\xi_1, \xi_2, \xi_3)$ is defined as

$$\vec{\omega} = \nabla\times\vec{v}. \tag{42}$$

To calculate velocity from vorticity, it is convenient to introduce a vector potential $\vec{\psi}=(\psi_1, \psi_2, \psi_3)$, which may be looked upon as the three-dimensional counterpart of two-dimensional stream function. The vector potential is defined by

$$\vec{v} = \nabla\times\vec{\psi}. \tag{43}$$

It easy to show the existence of such a vector potential for a solenoidal vector field ($\nabla\cdot\vec{v}=0$), which is required to be solenoidal, i.e.,

$$\nabla\cdot\vec{\psi} = 0. \tag{44}$$

Substituting Eq. (43) in Eq. (42) and using Eq. (44) yields

$$\nabla^2\vec{\psi} = -\vec{\omega}. \tag{45}$$

The set of Eqs. (9), (10), (41), (43) and (45) with appropriate boundary conditions form the basis for the numerical computations. The discretized form of these equations using second order finite difference scheme can be written as:

$$(\delta_x^2+\delta_y^2+\delta_z^2)\psi_{1ijk}^{n+1} = -\xi_{1ijk}^{n}, \tag{46}$$

$$(\delta_x^2+\delta_y^2+\delta_z^2)\psi_{2ijk}^{n+1} = -\xi_{2ijk}^{n}, \tag{47}$$

$$(\delta_x^2+\delta_y^2+\delta_z^2)\psi_{3ijk}^{n+1} = -\xi_{3ijk}^{n}, \tag{48}$$

$$u_{ijk}^{n+1} = \delta_y\psi_{3ijk}^{n+1} - \delta_z\psi_{2ijk}^{n+1}, \tag{49}$$

$$v_{ijk}^{n+1} = \delta_z\psi_{1ijk}^{n+1} - \delta_x\psi_{3ijk}^{n+1}, \tag{50}$$

$$u_{ijk}^{n+1} = \delta_x\psi_{2ijk}^{n+1} - \delta_y\psi_{1ijk}^{n+1}, \tag{51}$$

$$\left(\frac{1}{f_k}+M^2\right)\xi_{1ijk}^{n+1} = \frac{f_k'}{f_k^2}v_{ijk}^{n+1} + R\delta_y\theta_{ijk}^{n+1} - R_c\delta_y\phi_{ijk}^{n+1} + M^2\delta_y w_{i,j,k}^{n+1}, \tag{52}$$

$$\left(\frac{1}{f_k}+M^2\right)\xi_{2ijk}^{n+1} = -\frac{f_k'}{f_k^2}u_{ijk}^{n+1} - R\delta_x\theta_{ijk}^{n+1} + R_c\delta_x\phi_{ijk}^{n+1} - M^2\delta_x w_{i,j,k}^{n+1}, \tag{53}$$

$$\xi_{3ijk}^{n+1} = 0, \tag{54}$$

$$\frac{\theta_{ijk}^{n+1}-\theta_{ijk}^{n}}{\Delta t} + u_{ijk}^{n}\delta_x\theta_{ijk}^{n} + v_{ijk}^{n}\delta_y\theta_{ijk}^{n} + w_{ijk}^{n}\delta_z\theta_{ijk}^{n} + T_f\delta_z\theta_{ijk}^{n} = Rf_{1k}w_{ijk}^{n} + (\delta_x^2+\delta_y^2+\delta_z^2)\theta_{ijk}^{n}, \tag{55}$$

$$\hat{\varepsilon}\left(\frac{\phi_{ijk}^{n+1}-\phi_{ijk}^{n}}{\Delta t}\right) + u_{ijk}^{n}\delta_x\phi_{ijk}^{n} + v_{ijk}^{n}\delta_y\phi_{ijk}^{n} + w_{ijk}^{n}\delta_z\phi_{ijk}^{n} + T_f\delta_z\phi_{ijk}^{n} = R_c f_{2k}w_{ijk}^{n} + \frac{1}{Le}(\delta_x^2+\delta_y^2+\delta_z^2)\phi_{ijk}^{n}, \quad i,j,k=1,\ldots,m. \tag{56}$$

where δ_x^2, δ_y^2, δ_z^2 are the second-order central difference operators and δx, δy, δz are the first-order central difference operators. Here, u_{ijk}^{n+1}, v_{ijk}^{n+1}, w_{ijk}^{n+1}, ζ_{3ijk}^{n+1}, θ_{ijk}^{n+1} and ϕ_{ijk}^{n+1}, are computed explicitly from (49), (50), (51), (54), (55) and (56), respectively, while $\psi_{1i,j,k}^{n+1}$, $\psi_{2i,j,k}^{n+1}$, $\psi_{3i,j,k}^{n+1}$, ζ_{1ijk}^{n+1}, and ζ_{2ijk}^{n+1} are computed from (46), (47), (48), (52), and (53), respectively, implicitly using the Gauss-Seidel iteration method. The temperature and concentration on the boundary can be computed explicitly using (11).

Here, we should mention that our scheme is flexible for various Ra values and thus the grid resolution has been selected according to the Ra values. We decrease the values of Δx, Δy and Δz as the value of Ra increases. However, for this problem, we find that $\Delta x=\Delta y=\Delta z=0.02$ is enough to give us very accurate results.

NUMERICAL RESULTS

In this section, Ra_L, is the critical Rayleigh number for linear instability theory and Ra_E is the critical Rayleigh number for the global nonlinear stability theory. The corresponding critical wavenumbers of the linear instability and the global nonlinear stability will be denoted by a_L and a_E, respectively. In Table 1, we present

Table 1. Critical Rayleigh and wavenumbers of the linear instability and nonlinear stability theories for T_f=3, ε=0.1, λ=0.5, M^2=0 and ε_1=1

R_c	Ra_L	a_L^2	Ra_E	a_E^2
0	1267.260	23.836	656.928	14.197
6	1502.994	25.731	656.928	14.197
8	1584.707	23.899	656.928	14.197
12	1704.129	24.917	656.928	14.197
16	1852.505	25.979	656.928	14.197
20	2032.226	27.109	656.928	14.197

numerical results of the linear instability and non-linear stability analyses. The dimensions of the box, which are calculated according to the critical wavenumber, are shown in Table 1. We assume that the perturbation fields ($\mathbf{u}$, θ, ϕ, $\mathcal{P}$) are periodic in the x and y directions and denote by $\Omega=[0, 4\pi/a_x]\times[0, 4\pi/\sqrt{3}a_y]\times[0, 1]$ to be the periodicity cell, where a_x and a_y are the wavenumbers in the x and y directions, respectively. a_x and a_y are evaluated according to the critical wavenumbers a_L where $a^2{}_L=a^2{}_x+a^2{}_y$, where $Lx=4\pi/a_x$ and $Ly=4\pi/\sqrt{3}a_y$. These values of Lx and Ly are consistent with the hexagonal pattern of convection.

For numerical solutions in three dimensions, we used $\Delta t=5\times 10^{-5}$ and $\Delta x=\Delta y=\Delta z=0.02$. The convergence criterion have been selected to make sure that the solutions arrive at a steady state. The convergence criterion is

$$\chi=\max_{i,j,k}\{|\zeta^{n+1}_{1i,j,k}-\zeta^{n}_{1i,j,k}|, |\zeta^{n+1}_{2i,j,k}-\zeta^{n}_{2i,j,k}|, |\zeta^{n+1}_{3i,j,k}-\zeta^{n}_{3i,j,k}|, |\theta^{n+1}_{i,j,k}-\theta^{n}_{i,j,k}|, |\phi^{n+1}_{i,j,k}-\phi^{n}_{i,j,k}|\},$$

and we select $\chi=10^{-6}$. The program will continue computing the results for new time steps until the results satisfy the convergence criterion. Otherwise, if the solution cannot arrive at any steady state and oscillate, we present the results at τ=6, where τ is the measurement of the time.

To solve Eqs. (46)-(48) using the Gauss-Seidel iteration method, in the first time step we give an initial value to the potential vector and we denote $\psi^{1,k}_{1ijk}$, $\psi^{1,k}_{2ijk}$, $\psi^{1,k}_{3ijk}$ to be the potential vector. Then, using these initial values, we compute new values which we denote by $\psi^{1,k+1}_{1ijk}$, $\psi^{1,k+1}_{2ijk}$, $\psi^{1,k+1}_{3ijk}$ and use these values to evaluate new values. The program will continue in this process until the convergence criterion is satisfied, which is

$$\eta=\max_{i,j,k}\{|\psi^{1,k+1}_{1ijk}-\psi^{1,k}_{1ijk}|, |\psi^{1,k+1}_{2ijk}-\psi^{1,k}_{2ijk}|, |\psi^{1,k+1}_{3ijk}-\psi^{1,k}_{3ijk}|\}<10^{-5}.$$

In the next time steps, the values of ψ_{1ijk}, ψ_{2ijk}, ψ_{3ijk} in the time step n will be the initial values to the next time step.

Fig. 8 shows contour of perturbation velocity w at three locations in x−y plane z=0.05, z=0.5 and z=0.95, at τ=4, T_f=3, ε=0.1, λ=0.5, M^2=0 and ε_1=1. Fig. 8(a), (b) and (c) at R_c=0 and Ra=1268, while Fig. 8(d), (e) and (f) at R_c=12 and Ra=1705. The Figs. (a), (b) and (c) show multi cells symmetric in the shape about the center cell, where the center cell have two compound cells. These cells are negative sign and these symmetric because the periodic condition at the x and y sides of the problem. The minimum intensity of w at location z=0.5 (w_{min}=−20), this may be returned to far away from the disturbance of boundaries at z=0 & (d). In the Figs. (d), (e) and (f) the number of cells are increased, and become with two signs positive and negative (with sequence in the intensity and sign). This behavior because increase the value of R_c and Ra (R_c= 12 and Ra=1705), where the increase the effect of concentration and temperature with throughflow make the distribution of w is varying. The value of w are $w_{max}=3.7\times10^{-4}$, w_{max}=0.084, w_{max}=0.072 at (d), (e) and (f) respectively.

Fig. 9 clears contour of perturbation velocity w for three positions z=0.05, z=0.5 and z=0.95, at τ=4, R_c=20, T_f=3, ε=0.1, λ= 0.5, M^2=0 and ε_1=1, for two cases: (a), (b) and (c) at Ra=2000, and

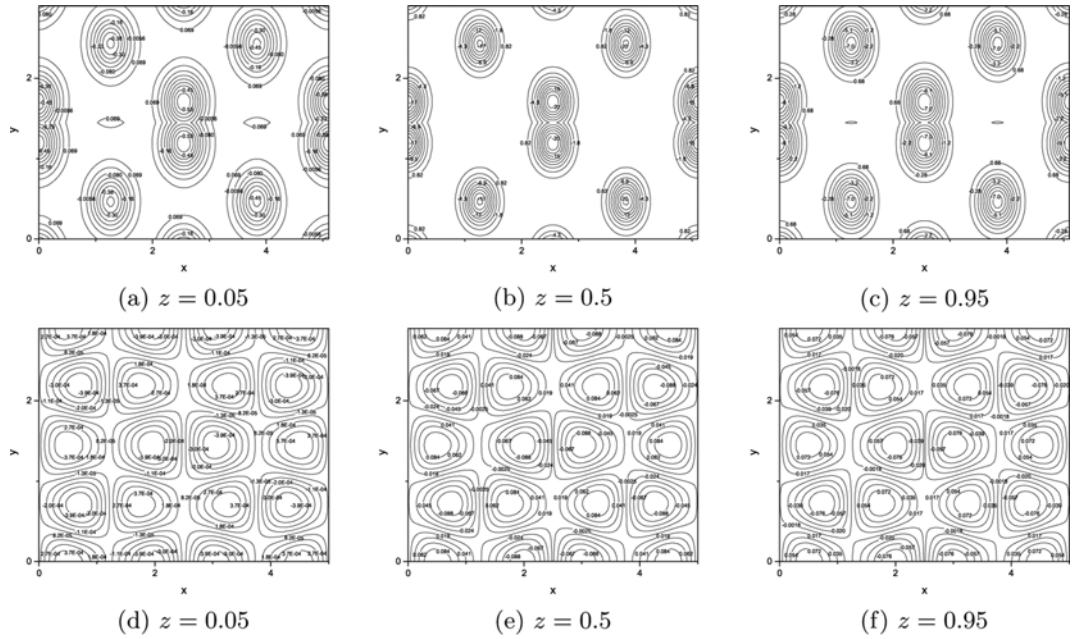

Fig. 8. Contour plot of w at τ=4, T_f=3, ε=0.1, λ=0.5, M^2=0 and ε_1=1. In (a), (b), (c) R_c=0 and Ra=1268. In (d), (e), (f) R_c=12 and Ra=1705.

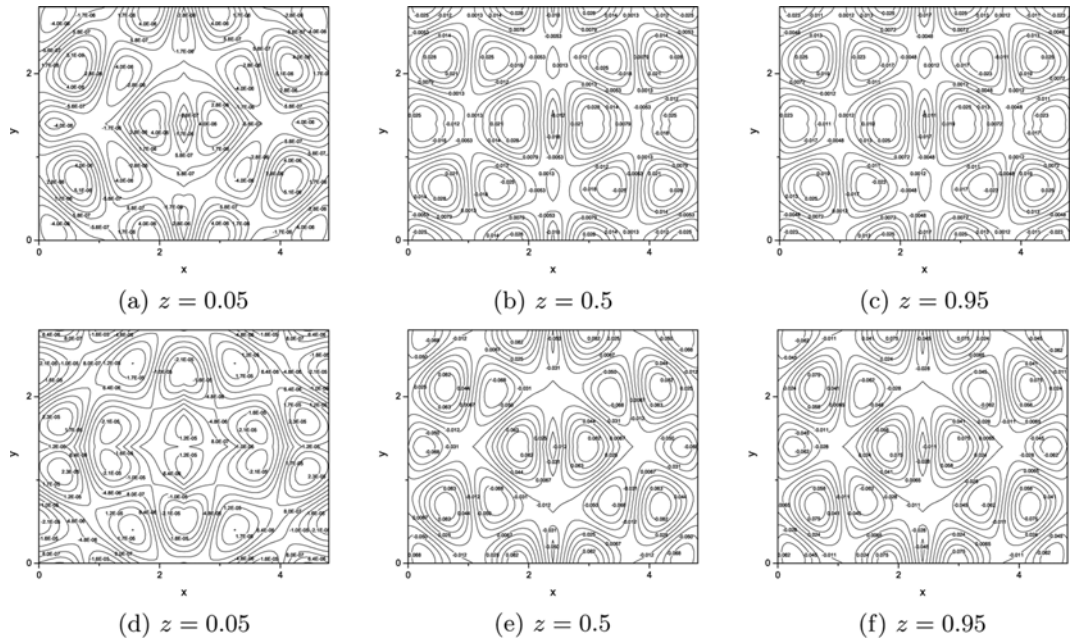

Fig. 9. Contour plot of w at τ=4, R_c=20, T_f=3, ε=0.1, λ=0.5, M^2=0 and ε_1=1. In (a), (b), (c) Ra=2000. In (d), (e), (f) Ra=2020.

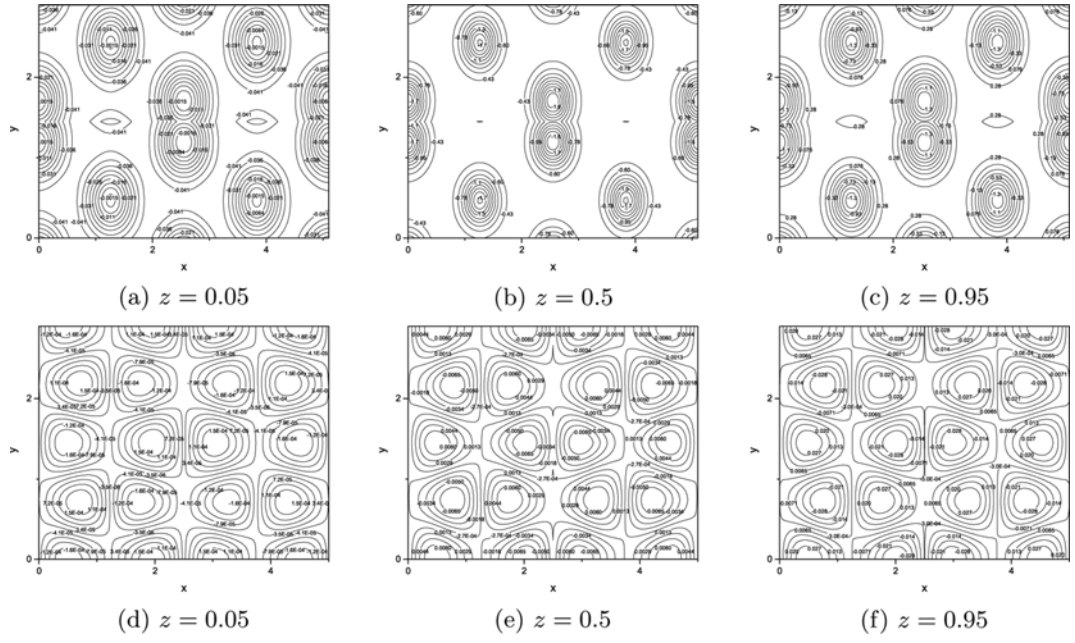

Fig. 10. Contour plot of θ at τ=4, T_f=3, ε=0.1, λ=0.5, M^2=0 and ε_1=1. In (a), (b), (c) R_c=0 and Ra=1268. In (d), (e), (f) R_c=12 and Ra=1705.

(d), (e) and (f) at Ra=2020. This figure show multi rotating cells with sequence symmetric in the intensity, shape and sign (positive and negative). It can be seen from the figure that the increase of Rayleigh number Ra gives increase the perturbation of w (positive and negative), which returned to increase temperature difference between lower plate (T_L) and upper plate (T_U), where $w_{max}=4\times10^{-6}$, $w_{max}=0.028$, $w_{max}=0.025$, $w_{max}=1.2\times10^{-5}$, $w_{max}=0.082$, $w_{max}=0.075$ at (a), (b), (c), (d), (e) and (f) respectively.

The contour of perturbation temperature θ is shown in the Fig. 10 for three locations in x–y plane z=0.05, z=0.5 and z=0.95, at τ=4, T_f=3, ε=0.1, λ=0.5, M^2=0 and ε_1=1. Fig. 10(a), (b) and (c) at R_c=0 and Ra=1268, while Fig. 10(d), (e) and (f) at R_c=12 and Ra=1705. It can be seen that the figures (a), (b) and (c) consist from multi cells of isotherm θ, the center cell have minimum magnitude and negative sign ($T=\overline{T}-\theta$). Also, the side cells are symmetric about the center cell, because the periodic condition at the x and y sides of the problem. The change of solute number R_c from 0 ((a), (b) & (c)) to 12 ((d), (e) & (f)) makes the cells dense and have sequence symmetric in the in the intensity, shape and sign (positive and negative). Also, the values of maximum and minimum

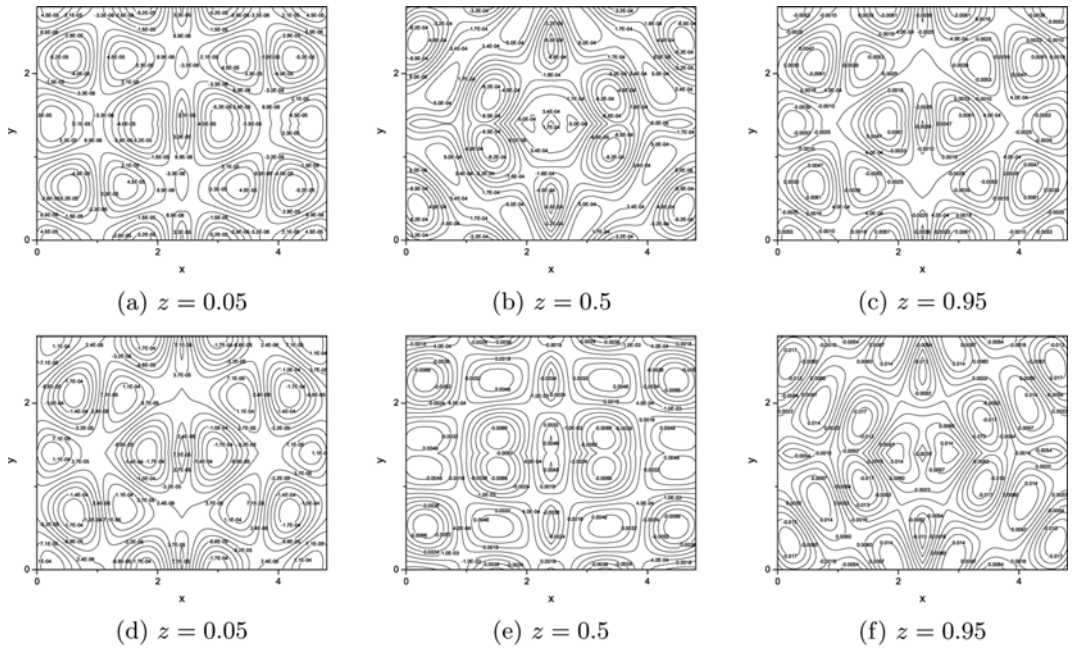

Fig. 11. Contour plot of θ at τ=4, R_c=20, T_f=3, ε=0.1, λ=0.5, M^2=0 and ε_1=1. In (a), (b), (c) Ra=2000. In (d), (e), (f) Ra=2020.

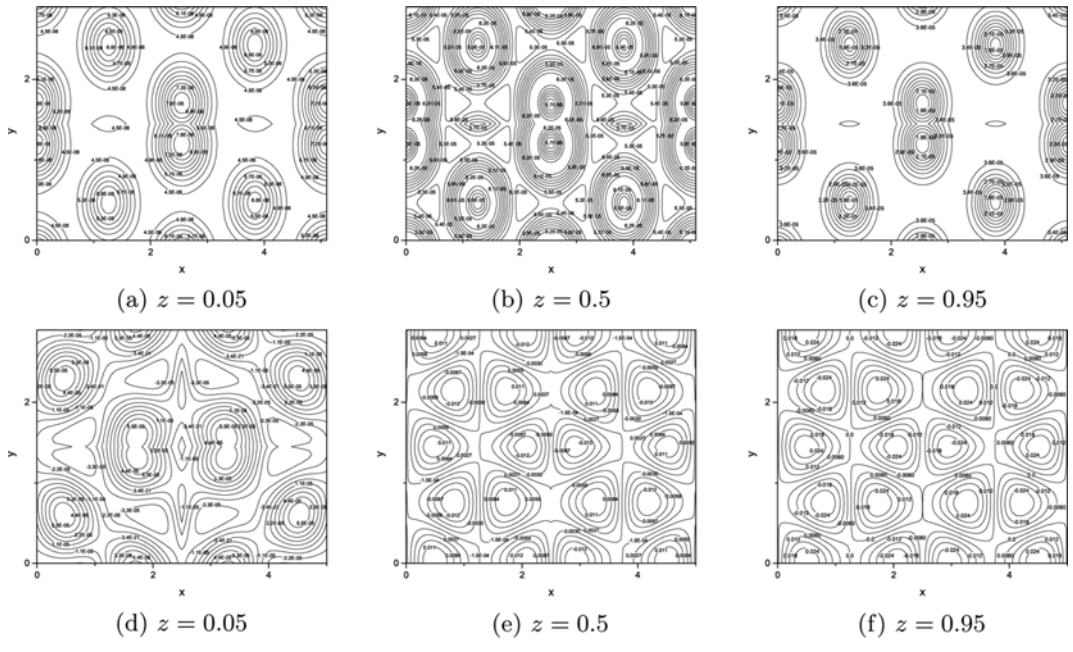

Fig. 12. Contour plot of ϕ at τ=4, T_f=3, ε=0.1, λ=0.5, M^2=0 and ε_1=1. In (a), (b), (c) R_c=0 and Ra=1268. In (d), (e), (f) R_c=12 and Ra=1705.

values of θ are lowered with increasing R_c, because increase the concentration difference ($C_L - C_U$), which increase the diusion.

The effect of increment of Rayleigh number Ra on θ is illustrated in Fig. 11, which plots the contour of θ at τ=4, R_c=20, T_f=3, ε=0.1, λ=0.5, M^2=0 and ε_1=1, for two cases: (a), (b) and (c) at Ra=2000, and (d), (e) and (f) at Ra=2020. From the figure, there are multi cells with sequence symmetric in the intensity, shape and sign (positive and negative). The values of maximum θ are: θ_{max}=4.5e−5, $\theta_{max}=1.7\times10^{-4}$, & θ_{max}=0.0061 at (a), (b) & (c) respectively, and $\theta_{max}=7.1\times10^{-4}$, θ_{max}=0.0046, θ_{max}=0.014 at (d), (e) and (f) respectively. It can be noted that θ_{max} increases with Ra, because increase the temperature difference (heat flow).

The Fig. 12 clears the contour of perturbation of concentrate ϕ at three locations z=0.05, 0.5 & 0.95, at τ=4, T_f=3, ε=0.1, λ=0.5, M^2=0 and ε_1=1. The contours of ϕ distribute as longitudinal cells with mirror images about x and y axises. These cells have positive sign ($C=\overline{C}+\phi$), and are: $\phi_{max}=7.6\times10^{-6}$, $\phi_{max}=5.9\times10^{-5}$, & $\phi_{max}=3.610\times10^{-5}$ at (a), (b) & (c) respectively. The boundary conditions of C ($C=C_L$ at z=0 and $C=C_U$ at z=d) make the diffusion of concentrate from lower surface to the upper surface and concentrated

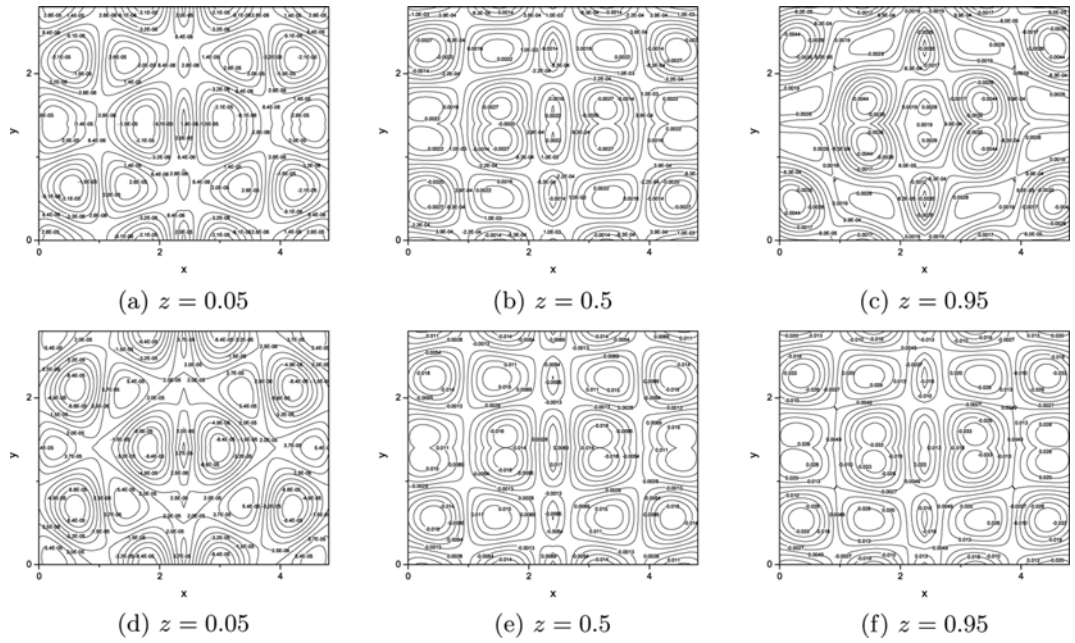

Fig. 13. Contour plot of ϕ at τ=4, R_c=20, T_f=3, ε=0.1, λ=0.5, M^2=0 and ε_1=1. In (a), (b), (c) Ra=2000. In (d), (e), (f) Ra=2020.

at the center of the box. Figs. (d), (e) & (f) show that the value and sign of the ϕ is varied with solute number R_c. This may be returned to increase the value of R_c and Ra (R_c=12 and Ra=1705), where throughflow make the distribution of ϕ is varying.

Finally, Fig. 13 illustrates the effect of varying Rayleigh number Ra ((a), (b) and (c) at Ra=2000, and (d), (e) and (f) at Ra=2020) on the contours of ϕ at τ=4, R_c=20, T_f=3; ε=0.1, λ=0.5, M^2=0 and ε_1=1. It can be noted that increase of Ra makes the cells of ϕ more dense with symmetric about x, y axises and diagonal. The minimum and maximum intensity of ϕ at ((a), (b) and (c)) lower than ϕ at ((d), (e) and (f)), because affect the density (ρ) with increasing Rayleigh number (temperatures differences ($T_L - T_U$). In general the solute and Rayleigh numbers have distinct effect on the distribution of w, θ and ϕ.

Figs. 14-19 show a summary of the numerical results where the maximum and minimum values of the third component of velocities versus time with T_f=3, ε=0.1, λ=0.5, M^2=0 and ε_1=1 are presented. The solid, dash, dot, dash dot, dash dot dot and short dash lines represent u_{max}, u_{min}, v_{max}, v_{min}, w_{max} and w_{min}, respectively. We repeated the experiment with M^2=1, and we found the behaviour of the stability is exactly similar to the case of M^2=0. The really interesting situation from both a geophysical and a mathematical viewpoint arises when the layer is simultaneously heated from below and salted from below. In this situation heating expands the fluid at the bottom of the layer and this in turn wants to rise thereby encouraging motion due to thermal convection. On the other hand, the heavier salt at the lower part of the layer has exactly the opposite effect and this acts to prevent motion through convective overturning. Thus, these two physical effects are competing against each other. Due to this competition, it means that the linear theory of instability does not always capture the physics of instability completely and (sub-critical) instabilities may arise before the linear threshold is reached. Due to the possibility of sub-critical instabilities occurring, it is very important to test the accuracy of the linear instability threshold in capturing the onset of the instability of the double diffusive problem when the layer is heated and salted from below.

In Figs. 14 and 15 R_c=0 and R_c=6, respectively, were chosen and for these cases the critical spectrum σ is found numerically to be always real. In Fig. 14, R_c=0 was selected, then, according to the stability analysis Ra_L=1267.26 and Ra_E=656.928 are obtained. Here, there is clearly a very large subcritical stability region as there is a

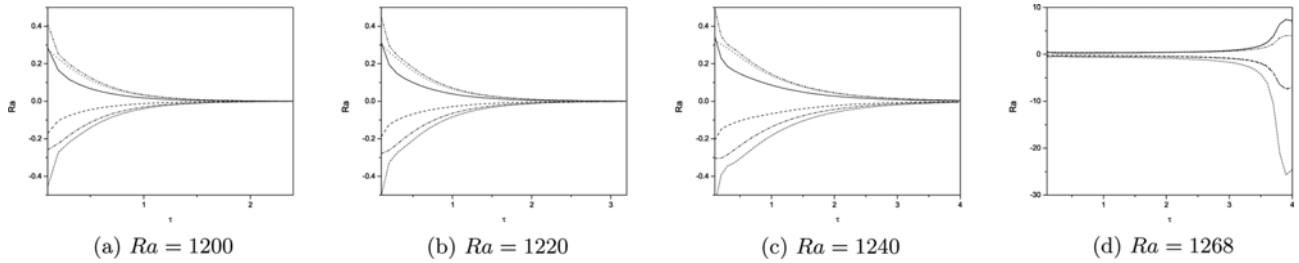

Fig. 14. The numerical results for different Ra. We present the results for the maximum and minimum values of velocities versus time for R_c=0. For this case Ra_L=1267.26, Ra_E=656.928.

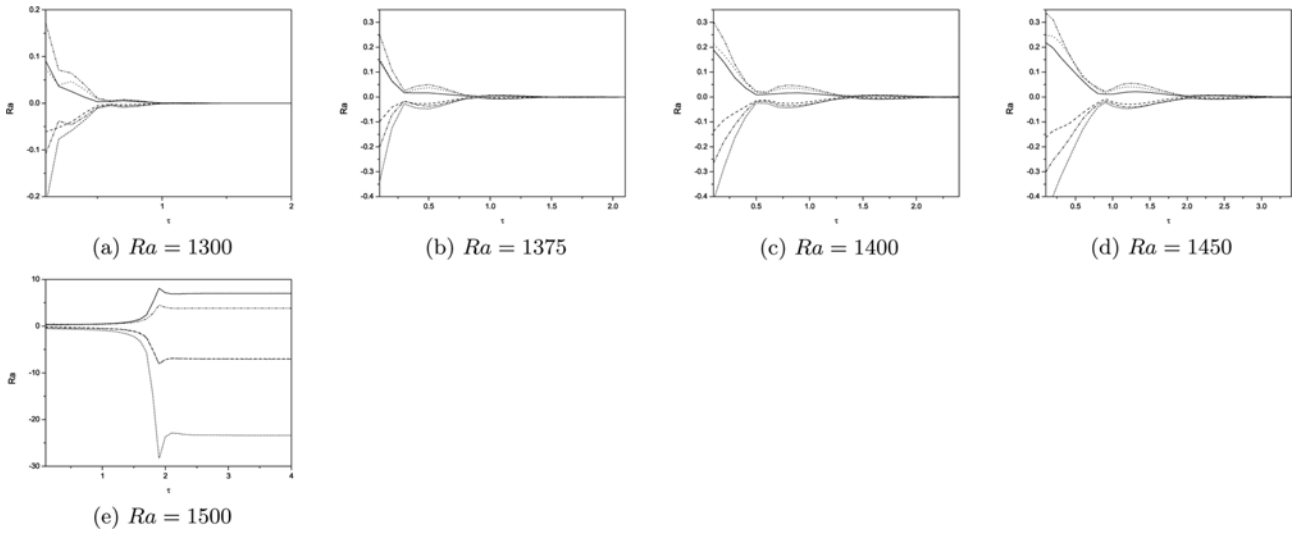

Fig. 15. The numerical results for different Ra. We present the results for the maximum and minimum values of velocities versus time for R_c=6. For this case Ra_L=1502.994, Ra_E=656.928.

big difference between the critical Rayleigh numbers of linear and nonlinear theories. From Fig. 14, for Ra=1200, it is evident that the values of velocity satisfy the convergence criteria at τ=2.439 and thus the solution arrives at the basic steady state within a short time. However, for Ra=1220, the program needs τ=3.2152 to arrive at the basic steady state, which is expected as the required time to arrive at a steady state increases with increasing Ra values until the solution does not reach to any steady state. Also, at Ra=1240, the basic steady state at τ=4 was not accessed. There was a decrease in the solutions values, however, and therefore accessing a basic steady state at future levels can be expected. Moreover, for Ra=1268, the solutions do not reach any steady state and the program stops at τ=4. For R^2=1268, the program was allowed to run for a significant period to test the convection's long time behaviour. It can be seen that the values of the velocities increase rapidly and continue in the oscillation behaviour. Here, according to the numerical results, the linear instability threshold is close to the actual threshold, i.e. the solutions reach the basic steady state before the linear instability threshold. The results in Fig. 15 indicate that the stability behaviour is similar to the stability behaviour of Fig. 14, as it was found that the actual threshold is close to the linear instability threshold. However, in Fig. 15, R_c=6 and thus the value of R_c very close to the switching point of convection from steady to oscillatory. In this case, the actual threshold will move slightly from the linear instability threshold.

At R_c=8, the nature of convection changes to oscillatory convection. For R_c=8 and R_c=12, the results are presented in Figs. 16 and 17, respectively, and in these cases, the numerical values of critical spectrum σ is always complex. In Fig. 16, critical Rayleigh numbers for R_c=8 were computed, the systems (39) and (38) were solved,

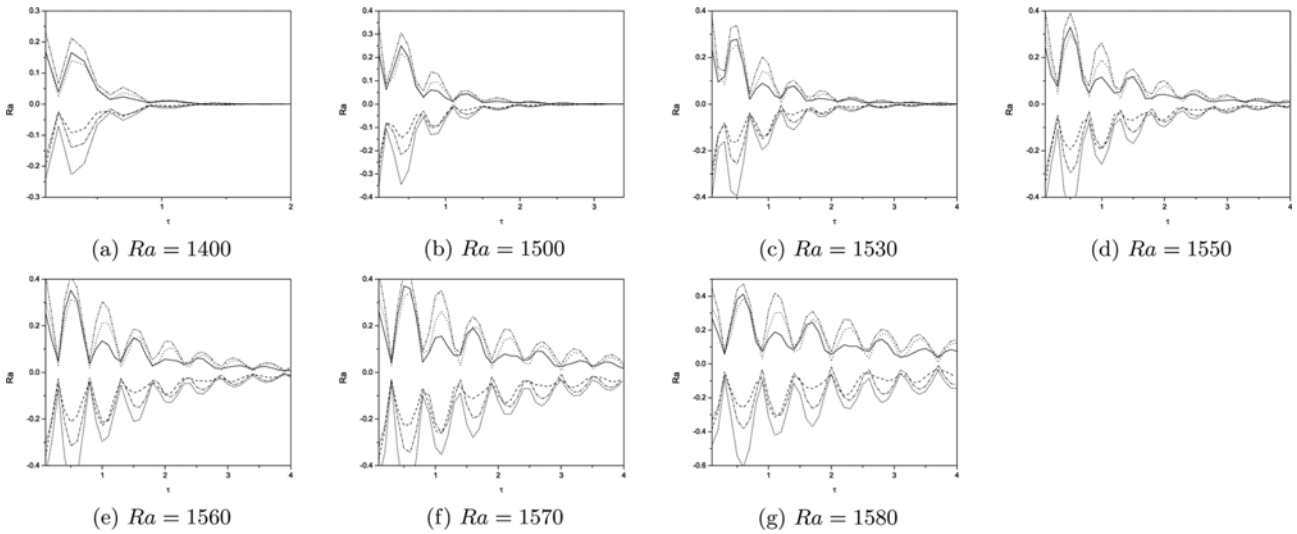

Fig. 16. The numerical results for different Ra. We present the results for the maximum and minimum values of velocities versus time for R_c=8. For this case Ra_L=1584.707, Ra_E=656.928.

leading to the following stability results: Ra_L=1584.707 and Ra_E= 656.928. In this case, the difference between the critical Rayleigh numbers of linear and nonlinear theories is very large. Fig. 16 shows that for Ra=1400 and Ra=1500 the solutions reach the basic steady state and satisfy the convergence criteria at τ=2.06455 and τ=3.44435, respectively. Moreover, at Ra=1530, the basic steady state at τ=4 could not be achieved, but there was a decrease in the solutions values and therefore reaching a basic steady state at the next time levels is expected. Also, for Ra=1550, Ra=1560, Ra=1570 and Ra= 1580, the solutions cannot achieve any steady state and the program stops at τ=4. For Ra=1550, Ra=1560, Ra=1570 and Ra=1580, the convection behaviour was very oscillated and access to a stable state was impossible. For Fig. 17, R_c=12 was selected, then the R_c value moved from the switching point of convection from steady to oscillatory. The results of Fig. 17 demonstrate that the stability behaviour is similar to the stability behaviour of Fig. 16, as it was found that the actual threshold is close to the linear instability threshold but only one difference. The difference is that the actual threshold move form the linear instability threshold. We can see from Fig. 16 that as the value of R_c moves from the switching point, the actual threshold will move from the linear instability threshold.

As R_c is increased, the oscillatory modes become present in the linear instability thresholds. The results for R_c=16 and R_c=20 in Figs. 18 and 19, respectively, are presented. Fig. 18, shows Rayleigh numbers for R_c=16, with solutions for systems (39) and (38), which produced the following stability results: Ra_L=1852.505 and Ra_E= 656.928. As can be seen, the difference between the critical Rayleigh numbers of linear and nonlinear theories is considerable, with Fig. 18 showing that for Ra=1600 and Ra=1750 the solutions achieve the basic steady state soon and satisfy convergence criteria at τ=

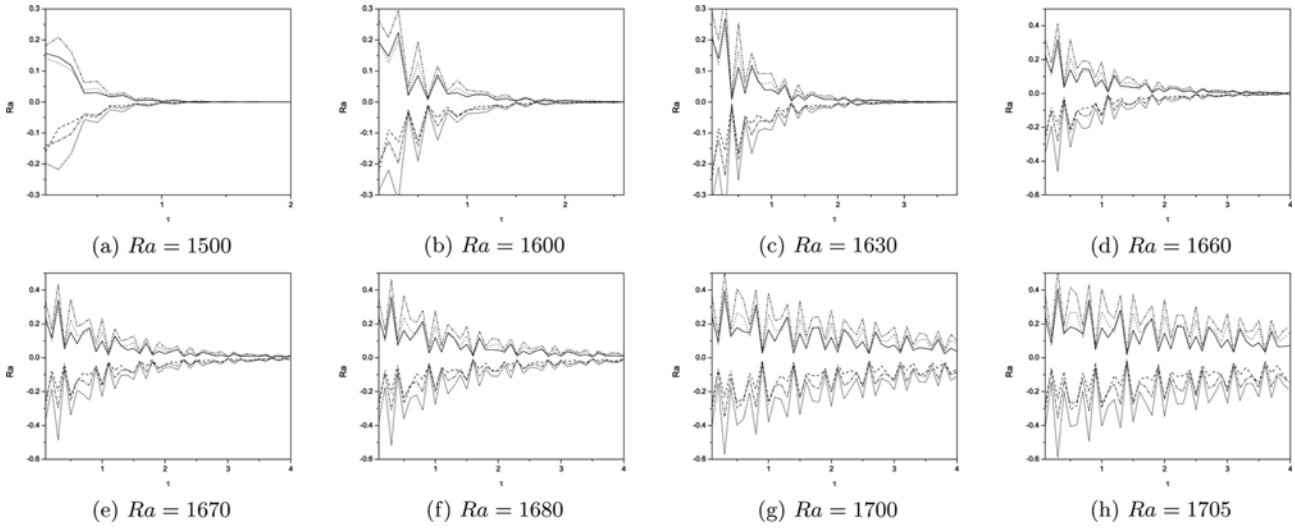

Fig. 17. The numerical results for different Ra. We present the results for the maximum and minimum values of velocities versus time for R_c=12. For this case Ra_L=1704.129, Ra_E=656.928.

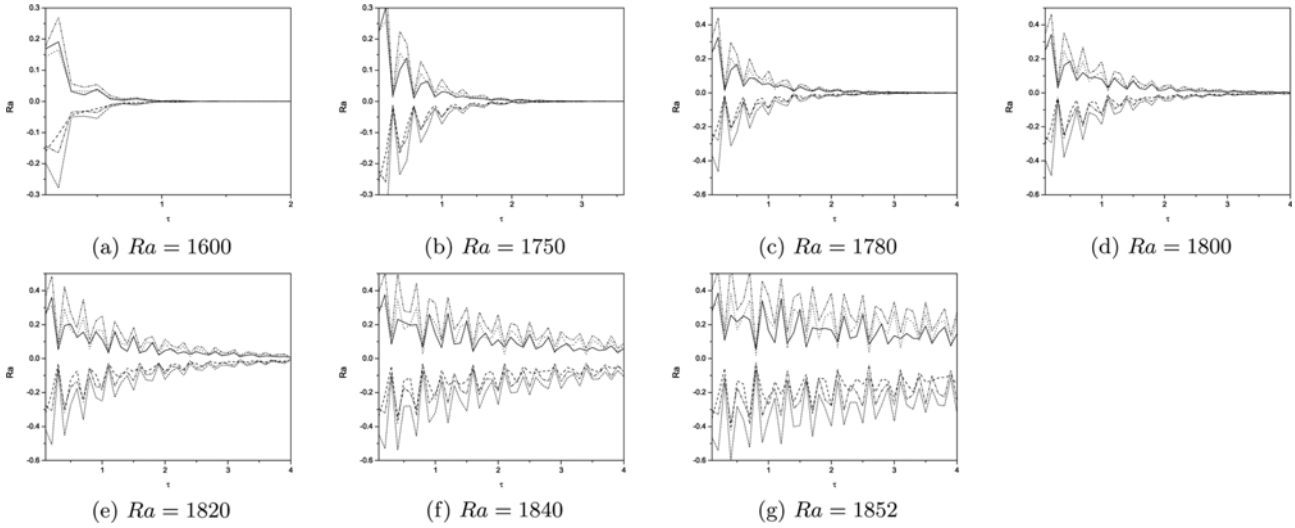

Fig. 18. The numerical results for different Ra. We present the results for the maximum and minimum values of velocities versus time for R_c=16. For this case Ra_L=1852.505, Ra_E=656.928.

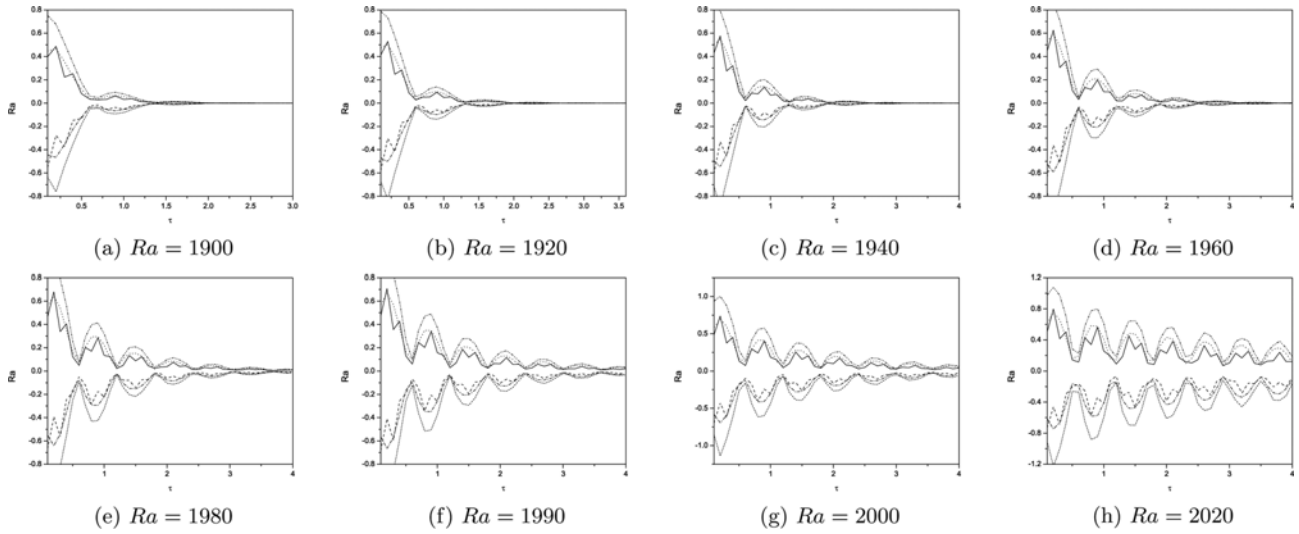

Fig. 19. The numerical results for different Ra. We present the results for the maximum and minimum values of velocities versus time for R_c=20. For this case Ra_L=2032.226, Ra_E=656.928.

2.00705 and τ=3.6226, respectively. Moreover, for Ra=1780 and Ra=1800, the solutions do not satisfy the convergence criterion and the program stops at τ=4, but it is clear that the solutions can achieve the convergence criterion on the next occasions. Furthermore, for Ra=1820, Ra=1840 and Ra=1852, the solutions could not reach any steady state and the program did not progress beyond τ=4. For Ra=1820, Ra=1840 and Ra=1852, the convection behaviour oscillated and access to a stable state was impossible. In Fig. 19, the value of R_c was 20. As previously mentioned, as the value of R_c increases, the actual threshold converges from the nonlinear stability threshold and the behaviour of the solutions becomes more oscillated.

CONCLUSIONS

In this paper we have explored double-diffusive convection in an anisotropic porous layer with a constant throughflow. Regions of very large subcritical instabilities, i.e. where agreement between the linear instability thresholds and nonlinear stability thresholds is poor, are studied by solving for the full three-dimensional system. The results indicate that the linear threshold accurately predicts on the onset of instability in the basic steady state. However, the required time to arrive at the steady state increases significantly as the Rayleigh number tends to the linear threshold.

We find that the linear instability threshold (Ra_L) gives an accurate prediction to the physical conditions under which the steady state throughflow will destabilise. If the Rayleigh number Ra is less than Ra_L, the temperature, velocity, vorticity and potential perturbations vanish, sending the solution back to the steady state, before the linear thresholds are reached. Numerically, the required time to arrive at the steady state increases as the value of Ra increases. When Ra is close to Ra_L, the solutions can tend to a steady state which is different to the basic steady state $\overline{v}$ =(0, 0, V). When Ra> Ra_L the steady state throughflow destabilises, with oscillating perturbations.

ACKNOWLEDGEMENTS

This work was supported by the Iraqi ministry of higher education and scientific research. Also, the authors would like to thank two anonymous referees for their pointed remarks that have led to improvements in the manuscript.

REFERENCES

1. A. J. Harfash, *Transp. Porous Media*, **103**, 361 (2014).
2. A. J. Harfash, *Transp. Porous Media* (2014), DOI:10.1007/s11242-014-0394-4.
3. A. J. Harfash, A. K. Alshara, *Korean J. Chem. Eng.*, (2015), DOI: 10.1007/s11814-014-0327-5.
4. D. A. Nield and A. Bejan, *Convection in Porous Media*, 4th Ed., Springer-Verlag, New York (2013).
5. D. A. Nield, *AIChE J.*, **33**, 1222 (1987).
6. I. S. Shivakumara, *Acta Mech.*, **37**, 151 (1999).
7. I. S. Shivakumara and C. E. Nanjundappa, *Archives of Mechanics*, **53**, 1 (2001).
8. I. S. Shivakumara and A. Khalili, *Transp. Porous Med.*, **53**, 245 (2003).
9. D. A. Nield, *The stability of convective flows in porous media*, In: Convective heat and mass transfer in porous media (S. Kakas et al., Eds.) **196**, 79 (1990).
10. N. Rudraiah, I. S. Shivakumara and R. Friedrich, *Int. J. Heat Mass Trans.*, **29**, 1301 (1986).
11. I. S. Shivakumara, *Further results on double diffusive magnetoconvection*, In: Recent advances in fluid mechanics (P. L. Sachdev, M. Venkatachalappa, Eds.), Gordon and Breach (1995).
12. I. S. Shivakumara and S. P. Suma, *Acta Mech.*, **140**, 207 (2000).
13. I. S. Shivakumara and A. Khalili, *Acta Mech.*, **152**, 165 (2001).
14. I. S. Shivakumara and S. Sureshkumar, *J. Geophys. Eng.*, **4**, 104 (2007).
15. D. A. Nield and A. V. Kuznetsov, *Transp. Porous Med.*, **87**, 765

(2011).
16. A. A. Hill, S. Rionero and B. Straughan, *IMA J. Appl. Math*., **72**, 635 (2007).
17. A. J. Harfash and A. A. Hill, *Int. J. Heat Mass Trans*., **72**, 609 (2014).
18. B. Straughan, *The energy method, stability, and nonlinear convection*, Applied Mathematical Sciences, Second Ed., **91**, Springer (2004).
19. P. Ganesan and R. K. Suganthi, *Korean J. Chem. Eng*., **30**, 813 (2013).
20. I. G. Hwang, *Korean J. Chem. Eng*., **30**, 1023 (2013).
21. M. C. Kim, *Korean J. Chem. Eng*., **30**, 831 (2013).
22. M. C. Kim, *Korean J. Chem. Eng*., **30**, 1207 (2013).
23. M. C. Kim and C. K. Choi, *Int. J. Heat Mass Transfer*, **71**, 313 (2014).
24. Q. Liu, D. Shen, R. Xiao, H. Zhang and M. Fang, *Korean J. Chem. Eng*., **30**, 613 (2013).
25. M. Lungu, J. Sun, J. Wang, Z. Zhu and Y Yang, *Korean J. Chem. Eng*., **31**, 1148 (2014).
26. D. A. Nield and A. V. Kuznetsov, *Transp. Porous Media*., **102**, 1 (2014).
27. D. A. Nield and A. V. Kuznetsov, *Transp. Porous Media*., **102**, 15 (2014).
28. N. Sharma, A. t Dhiman and S. Kumar, *Korean J. Chem. Eng*., **31**, 754 (2014).
29. M. Shojaeian and S. M. N. Shojaee, *Korean J. Chem. Eng*., **30**, 823 (2013).
30. B. Straughan, *Microfluid Nanofluid*, **16**, 361 (2014).
31. B. Straughan, *Acta Appl. Math*. (2014), DOI:10.1007/s10440-014-9930-z.
32. A. J. Harfash, *Transp. Porous Media*, **101**, 281 (2014).
33. A. J. Harfash, *Appl. Math. Comput*., **227**, 92 (2014).
34. A. J. Harfash, *Transp. Porous Media*, **102**, 43 (2014).
35. A. J. Harfash, *Acta Mechanica Sinica*, **30**, 144 (2014).
36. A. J. Harfash, *J. Non-Equilib. Thermodyn*. (2014), DOI:10.1515/jnet-2014-0009.
37. G. P. Galdi and B. Straughan, *Arch. Rational Mech. Anal*., **89**, 211 (1985).
38. P. H. Roberts, *An introduction to magnetohydrodynamics*, Longman, London (1967).
39. M. Fabrizio and A. Morro, *Electromagnetism of continuous media*, Oxford University Press, Oxford (2003).
40. D. D. Joseph, *Arch. Rational Mech. Anal*., **35**, 169 (1969).
41. A. J. Harfash, *Stability analysis for penetrative convection in a fluid layer with throughflow, Submited to European J. Mech. - B/Fluids*.